

ANALYSIS OF SUPERSONIC FLOW OVER A DOUBLE WEDGE AEROFOIL

A Multi-Method Approach to Supersonic Aerodynamics

Abstract

The supersonic flow field over a double wedge aerofoil is investigated using theoretical analysis, CFD simulation, and experimental techniques. Shock wave relations and Prandtl-Meyer functions are used for theoretical predictions. CFD simulations are conducted to model the flow, and experimental data is analysed from Schlieren images and pressure measurements. This study compares the shock wave and expansion fan angles and pressure distributions obtained from each method, discussing any discrepancies and their possible causes, thus providing a comprehensive validation and understanding of supersonic flow phenomena around the aerofoil.

Table of Contents

1	Theoretical Analysis	1-2
1.1	Shock-Expansion Theory Analysis	2-3
1.2	Lift Coefficient (CL) and Wave-Drag Coefficient (CD)	2-5
1.3	Sketch	2-6
2	Numerical Analysis (CFD):	3-6
2.1	CFD Setup	3-6
2.2	Convergence	3-9
2.3	Post-Processing	3-10
2.4	Pressure Data Extraction	3-12
2.5	Angle Measurement	3-12
3	Experimental Analysis:	4-13
3.1	Schlieren Image Analysis	4-14
3.2	Pressure Data Analysis	4-15
3.3	Discussion of Trends:	4-16
4	Results Comparison and Discussion:	5-16
4.1	Angle Comparison	5-16
4.2	Pressure Comparison	5-17
5	Conclusion	6-19
	Figure 1 Flow features around a double-wedge aerofoil in supersonic flow ($M>1$) at an angle of attack.	1-3
	Figure 2 Diagram of Aerofoil in Wind Tunnel	1-3
	Figure 3 Sketch illustrating the theoretical wave pattern around the double-wedge aerofoil at $M=1.8$ and 5° AoA, based on Shock-Expansion theory, showing distinct flow regions and wave structures	2-6
	Figure 4 2D computational domain representing the wind tunnel test section	3-7
	Figure 5 Full structured mesh of Geometry	3-7
	Figure 6 Zoomed image of mesh around the double wedge Aerofoil	3-7
	Figure 7 Boundary Conditions	3-8
	Figure 8 Convergence of Simulation	3-9
	Figure 9 Mach Number Contour Plot	3-10
	Figure 10 - Pressure Coefficient Contour Plot	3-11
	Figure 11 Pressure Coefficient vs. Position Plot as Figure	3-12
	Figure 12 Schlieren Image Setup	4-13
	Figure 13 AF300 Wind Tunnel	4-13
	Figure 14 Schlieren Image	4-14

1 Introduction

The study of supersonic flow is fundamental to the design and analysis of high-speed aerospace vehicles, missiles, and engine inlets. Understanding the complex flow phenomena that arise when an object travels faster than the speed of sound, such as the formation of shock waves and expansion fans, is crucial for predicting aerodynamic performance and structural loads. The double-wedge aerofoil, while geometrically simple, serves as a canonical problem in supersonic aerodynamics, generating these characteristic features in a well-defined manner.

This report presents a comprehensive investigation into the two-dimensional supersonic flow field around a double-wedge aerofoil, characterised by a 10° total wedge angle, at a freestream Mach number of $M = 1.8$ and a 5° angle of attack (α). The primary goal is to analyse and compare the flow structure, specifically the leading-edge shock wave angles and the surface pressure coefficient (C_p) distribution, using three distinct methodologies: theoretical analysis, computational fluid dynamics (CFD), and experimental measurement.

A multi-method approach provides valuable insights not achievable through a single technique. Theoretical analysis, employing Shock-Expansion theory, offers analytical predictions based on idealized inviscid flow assumptions. Computational Fluid Dynamics (CFD), utilizing ANSYS Fluent with the Spalart-Allmaras turbulence model, provides a detailed numerical simulation of the viscous flow field. Experimental analysis examines data acquired from the TecQuipment AF300 intermittent supersonic wind tunnel, including Schlieren flow visualization and direct surface pressure measurements.

By comparing the results obtained from these three approaches, this study aims to:

1. Characterize the supersonic flow field around the specified double-wedge airfoil configuration.
2. Quantify key parameters including shock wave angles and pressure coefficients using each method.
3. Evaluate the level of agreement and identify discrepancies between theoretical predictions, numerical simulations, and experimental data.
4. Discuss potential reasons for observed discrepancies, considering the inherent assumptions and limitations of each methodology.

This comparative analysis serves to validate the different methods against each other and provides a deeper understanding of the physical phenomena governing supersonic flow over wedge-shaped bodies. The report is structured to first present the findings from the theoretical analysis, followed by the CFD simulation setup and results, and then the experimental data analysis. Subsequently, a dedicated section compares and discusses the results across all three methods, leading into the final conclusions of the study.

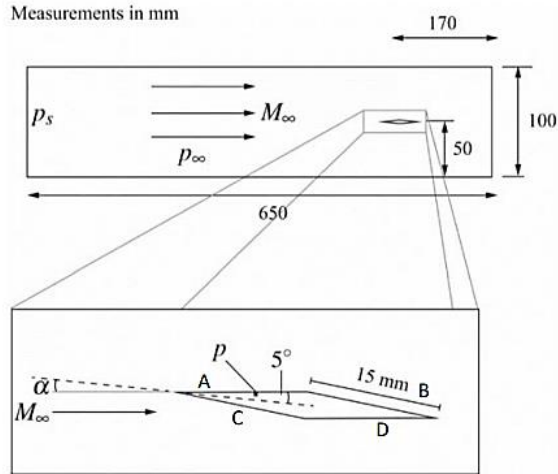


Figure 2 Diagram of Aerofoil in Wind Tunnel

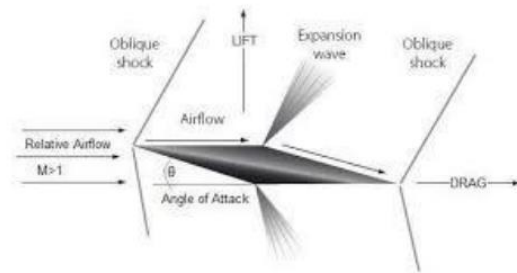


Figure 1 Flow features around a double-wedge aerofoil in supersonic flow ($M > 1$) at an angle of attack.

2 Theoretical Analysis

This section presents the theoretical analysis of supersonic flow at Mach $M_1 = 1.8$ over a double-wedge aerofoil with a 10° total wedge angle at a 5° angle of attack (α). Shock-Expansion theory, which accounts for non-linear compressibility effects through discrete shock waves and Prandtl-Meyer expansion fans originating from the aerofoil corners, is employed. This method provides predictions for the surface pressure distribution and the angles of the resulting wave patterns. The ratio of specific heats for air is taken as $\gamma = 1.4$.

2.1 Shock-Expansion Theory Analysis

Region 1: Freestream Conditions

Description: The flow is parallel to the freestream with no turning, maintaining the freestream conditions.

Flow Properties:

Turning angle: $\theta_1 = 0^\circ$

Mach number: $M_1 = M_\infty = 1.8$

Pressure coefficient: $C_{p1} = 0$ (indicating no pressure change)

$$\mu_1 = \sin^{-1}\left(\frac{1}{M_\infty}\right) = \sin^{-1}\left(\frac{1}{1.8}\right) = 33.75^\circ$$

Region 2: Expansion Fan Due to Flow Turning Away

Description: The flow turns away from the freestream by 10° , producing an expansion fan at the corner.

Mach Number Calculation:

$$v(M_2) - v(M_1) = \Delta$$

$$v(M_1) = v(1.8) = 20.7251^\circ$$

$$v(M_2) = 10^\circ + 20.7251^\circ = 30.7251^\circ \approx 30.751^\circ$$

By interpolation: $M_2 \approx 2.1624$

Pressure Calculation:

$$\frac{p_2}{p_\infty} = \frac{p_2/p_{t2}}{p_\infty/p_{t1}} = \frac{0.0992}{0.1740} = 0.570$$

Pressure Coefficient:

$$C_{p,2} = \frac{\left(\frac{p_2}{p_\infty} - 1\right)}{\frac{\gamma}{2} M_\infty^2} = \frac{0.570 - 1}{\frac{1.4}{2} \cdot 1.8^2} = -0.1896$$

Region 3: Oblique Shock Due to Flow Turning into Freestream

Description: The flow turns into the freestream by 10° , generating an oblique shock at the leading edge.

Flow Properties:

Shock wave angle: $\beta = 44.03425^\circ$

Mach number after the shock: $M_3 = 1.4524$

Pressure Calculation:

$$\frac{p_3}{p_\infty} = \frac{p_3/p_{t3}}{p_\infty/p_{t1}} = \frac{0.2917}{0.1740} = 1.6764$$

Pressure Coefficient:

$$C_{p,3} = \frac{\left(\frac{p_3}{p_\infty} - 1\right)}{\frac{\gamma}{2} M_\infty^2} = \frac{1.6764 - 1}{\frac{1.4}{2} \cdot 1.8^2} = 0.2982$$

Region 4: Expansion Fan from Region 3

Description: The flow turns away from the direction in Region 3 by 10° , creating another expansion fan.

Mach Number Calculation:

$$v(M_4) - v(M_3) = \Delta$$

$$v(M_3) = v(1.4524) = 10.5085^\circ$$

$$v(M_4) = 10^\circ + 10.5085^\circ = 20.5085^\circ$$

By interpolation: $M_4 \approx 1.7925$

Pressure Calculation:

$$\frac{p_4}{p_\infty} = \frac{p_4}{p_{t4}} \cdot \frac{1}{p_3/p_{t3}} \cdot \frac{p_3}{p_\infty} = 0.1760 \cdot \frac{1}{0.2917} \cdot 1.6764 = 1.012$$

Pressure Coefficient:

$$C_{p,4} = \frac{\left(\frac{p_4}{p_\infty} - 1\right)}{\frac{\gamma}{2} M_\infty^2} = \frac{1.012 - 1}{\frac{1.4}{2} \cdot 1.8^2} = 0.005291$$

2.2 Lift Coefficient (CL) and Wave-Drag Coefficient (CD)

Lift Coefficient (CL)

The lift coefficient is calculated using the pressure coefficients from the four regions of the flow. The formula is:

$$CL = \frac{2}{L} \cos(5^\circ) (-C_{p,1} - C_{p,2} \cos(10^\circ) + C_{p,3} \cos(10^\circ) + C_{p,4})$$

Substituting the given values:

$$C_{p,1} = 0, \quad C_{p,2} = -0.1896, \quad C_{p,3} = 0.2982, \quad C_{p,4} = 0.005291$$

Simplifying:

$$CL = \frac{2}{L} \cos(5^\circ) (0.1896 \cos(10^\circ) + 0.2982 \cos(10^\circ) + 0.005291)$$

Using approximations: $\cos(5^\circ) \approx 0.9962$ and $\cos(10^\circ) = 0.9848$

$$CL = \frac{1}{2 \cdot 0.9962} (0.1896 \cdot 0.9848 + 0.2982 \cdot 0.9848 + 0.005291)$$

$$CL = \frac{1}{1.9924} (0.1867 + 0.2937 + 0.005291)$$

$$CL = \frac{0.485691}{1.9924} = 0.2438$$

Thus, the lift coefficient is:

$$CL = 0.2438$$

Theoretical Lift Coefficient

$$CL = \frac{4\alpha}{M_\infty^2 - 1}$$

Given: $\alpha = 5^\circ = 0.0872664626$ radians, $M_\infty = 1.8$

$$CL = \frac{4 \cdot 0.0872664626}{3.24 - 1} = \frac{0.3490658504}{2.24} = 0.2332$$

Thus, the theoretical lift coefficient is:

$$CL \approx 0.2332$$

Wave-Drag Coefficient (CD)

$$CD = \frac{4\alpha^2}{M_\infty^2 - 1} + \frac{2}{M_\infty^2 - 1} (\overline{\sigma}_l^2 + \overline{\sigma}_u^2)$$

First Term

$$\alpha = 0.0872664626 \text{ rad}, M_\infty = 1.8$$

$$\frac{4 \cdot (0.0872664626)^2}{3.24 - 1} = \frac{0.030461742}{1.497} = 0.02035$$

Second Term

$$\overline{\sigma_l^2} = \overline{\sigma_u^2} = (0.0872664626)^2 = 7.61 \times 10^{-3}$$

$$\overline{\sigma_l^2} + \overline{\sigma_u^2} = 1.522 \times 10^{-2}$$

$$\frac{2}{1.497} \cdot 1.522 \times 10^{-2} = 0.02034$$

Total Wave-Drag Coefficient

$$CD = 0.02035 + 0.02034 = 0.04069$$

Thus, the wave-drag coefficient is:

$$CD = 0.04069$$

2.3 Sketch

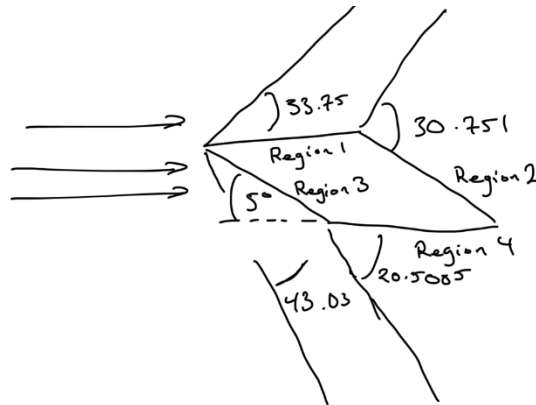


Figure 3 Sketch illustrating the theoretical wave pattern around the double-wedge aerofoil at $M=1.8$ and 5° AoA, based on Shock-Expansion theory, showing distinct flow regions and wave structures

3 Numerical Analysis (CFD):

3.1 CFD Setup

Computational Fluid Dynamics (CFD) analysis was performed to simulate the supersonic flow (Mach 1.8) over the specified double-wedge airfoil (10° wedge angle, 20.5mm chord) at a 5° angle of attack within a 101.6mm high channel. The analysis utilised the ANSYS Workbench 2025 R1 platform, integrating DesignModeler for geometry, ANSYS Meshing for mesh generation, and ANSYS Fluent for the flow simulation.

Computational Domain:

A 2D computational domain representing the wind tunnel test section was created. The channel height was maintained at 101.6mm. The domain extended 350mm upstream of the airfoil leading edge and 350mm

downstream to ensure that boundary conditions did not unduly influence the flow field near the airfoil. The airfoil was positioned centrally within the channel at a 5° angle of attack relative to the horizontal channel axis.

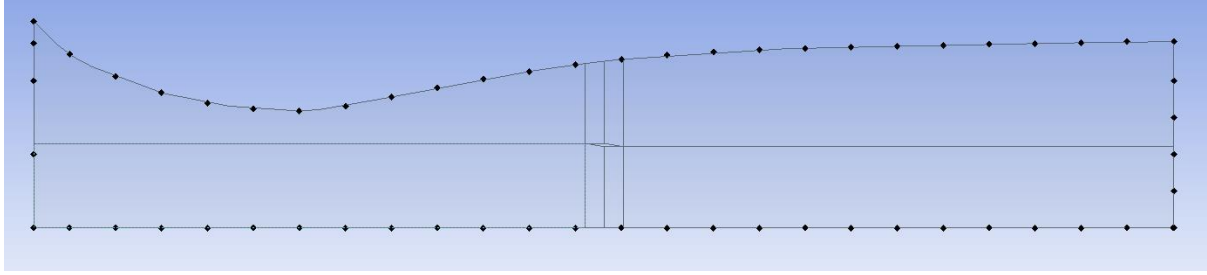


Figure 4 2D computational domain representing the wind tunnel test section

Meshing:

The mesh was generated using ANSYS Meshing tools. A structured meshing approach was prioritised where feasible using **Mapped Face Meshing** with quadrilateral elements, particularly in the regions adjacent to the airfoil and along the main channel path, aiming to enhance solution accuracy and alignment with the flow direction. To capture the high-gradient regions near the airfoil surfaces (boundary layer, shocks, expansion fans) efficiently, **Edge Sizing** was applied normal to the airfoil walls with a significant **Bias Factor** of 200. This strategy concentrates computational cells in the critical near-field region while allowing for rapid coarsening towards the far-field boundaries, optimising the balance between accuracy and computational expense as demonstrated in the course example. Explicit inflation layer controls were not utilised in this specific meshing setup, adhering to the procedure demonstrated; the necessary near-wall resolution was achieved through the application of the strong bias factor. The final mesh consisted of approximately 960000 elements. A visual representation of the mesh is provided in Figure 5 and 6.

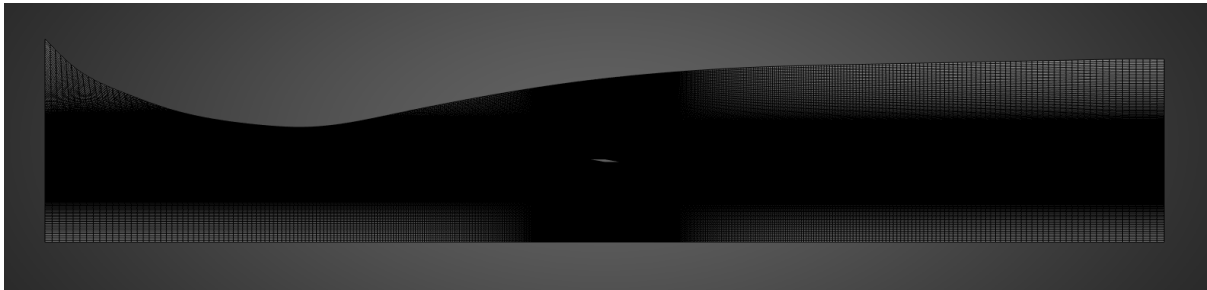


Figure 5 Full structured mesh of Geometry

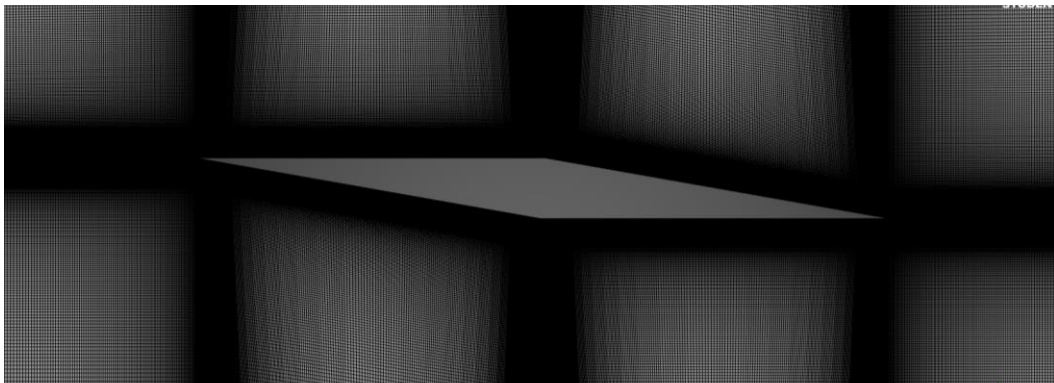


Figure 6 Zoomed image of mesh around the double wedge Aerofoil

- *Mesh Independence Note:* While a mesh independence study is crucial for rigorous CFD analysis, for the purpose of this specific learning exercise and to strictly follow the scope outlined in the provided lecture demonstration, a formal mesh independence study was not performed. The presented results are based on the mesh generated according to the demonstrated procedure.

Boundary Conditions:

The following boundary conditions were applied to the domain edges:

- **Inlet:** A **Pressure Far-Field** condition was applied at the start of the wind tunnel geometry. This allowed for the direct specification of the undisturbed upstream Mach number ($Ma = 1.8$) and static temperature ($T_{static} = 300K$).
- **Outlet:** A **Pressure Outlet** condition was applied downstream. The gauge pressure was set to 0 to allow the flow to exit the domain with minimal numerical reflections.
- **Airfoil Surfaces:** Defined as stationary **Wall** boundaries with a no-slip shear condition imposed. An adiabatic thermal condition (zero heat flux) was assumed.
- **Top and Bottom Channel Walls:** These are also defined as stationary wall boundaries with no-slip shear conditions and adiabatic thermal conditions.

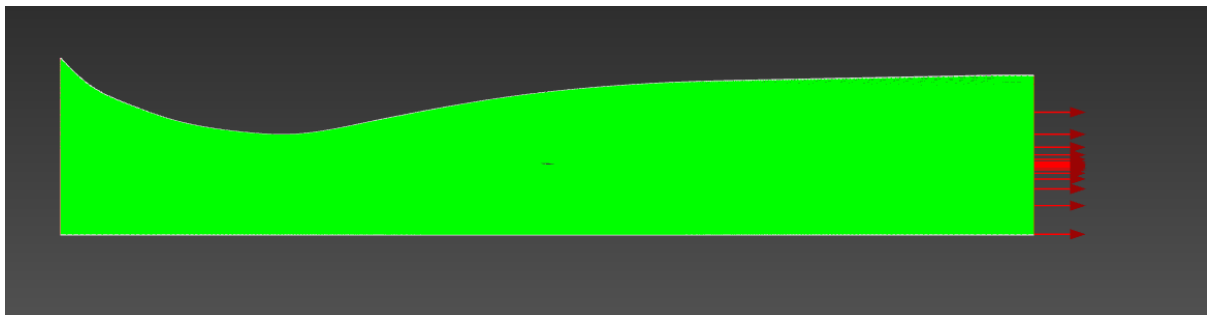


Figure 7 Boundary Conditions

Solver Settings:

The simulation was configured within ANSYS Fluent using the following settings:

- **Solver Type:** A **Pressure-Based** coupled solver was employed. While density-based solvers are often favored for supersonic flows, modern pressure-based algorithms within Fluent can robustly handle compressible flows in the lower supersonic regime ($Ma < 3$), offering good stability and convergence characteristics for this specific case, consistent with the course methodology.
- **Governing Equations:** The steady-state, 2D Reynolds-Averaged Navier-Stokes (RANS) equations were solved. The **energy equation was enabled to account for compressibility effects and temperature variations accurately.**

- **Fluid Properties:** The working fluid was defined as air and treated as an ideal gas to model compressibility. The molecular viscosity was calculated using the **Sutherland** law to account for its dependence on temperature.
- **Turbulence Model:** The **Spalart-Allmaras** one-equation turbulence model was selected. This model is computationally efficient and known for its robustness, particularly for external aerodynamic flows with attached boundary layers, making it suitable for this simulation scope and aligning with the methodology presented in the course materials.
- **Spatial Discretization:** To ensure accuracy, **Second Order Upwind** schemes were applied for the convection terms of the flow variables (momentum, energy) and the turbulence model equation. The **Roe-FDS** (Roe-Flux-Difference Splitting) scheme was used for flux calculations. Gradients were computed using the **Least Squares Cell-Based** method.

These setup choices were made to balance accuracy, computational efficiency, and robustness while adhering to the procedures demonstrated in the associated course materials for simulating this specific wind tunnel flow scenario.

3.2 Convergence

The convergence of the CFD simulation was carefully monitored to ensure a stable and reliable steady-state solution was achieved. The primary method for assessing convergence was tracking the scaled residuals for the governing equations throughout the iterative solution process.

Figure 6 displays the history of the scaled residuals for continuity, x-velocity, y-velocity, energy, and the Spalart-Allmaras turbulence variable (nut) plotted against the number of solver iterations.

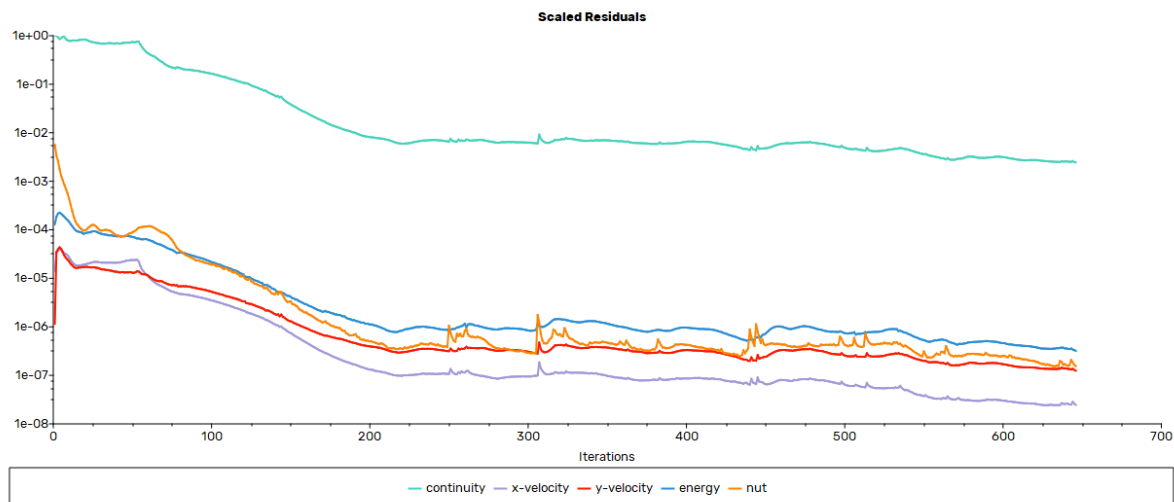


Figure 8 Convergence of Simulation

The convergence criteria were set such that the scaled residuals for all equations should ideally drop below 1×10^{-5} and exhibit stable, non-oscillating behaviour.

Observing Figure 8:

- All residuals show a significant decrease from their initial values, indicating the solver is progressing towards a solution.
- The residuals for x-velocity, y-velocity, energy, and the turbulence variable 'nut' all decrease substantially, reaching values well below 1×10^{-6} by approximately 650 iterations. These residuals also flatten out, indicating stability in the solution of these transport equations.
- The continuity residual decreases initially but levels off at a higher value, fluctuating around 1×10^{-2} to 5×10^{-3} . While this is higher than the target for other residuals, it exhibits stable, flattened behaviour, suggesting that the mass imbalance is no longer changing significantly. For complex supersonic flows, achieving very low continuity residuals can sometimes be challenging.

Based on the low levels achieved by the momentum, energy, and turbulence residuals (well below 1×10^{-6}) and the stable, flattened behaviour of *all* residuals, including continuity, the solution was considered converged after approximately **650 iterations**. This provides confidence that the presented post-processing results represent a numerically stable, steady-state solution to the governing equations for this flow problem.

3.3 Post-Processing

Post-processing of the converged CFD solution was performed using ANSYS Fluent's visualisation tools to analyse the flow field characteristics. Key flow features were visualised using contour plots generated from the simulation data.

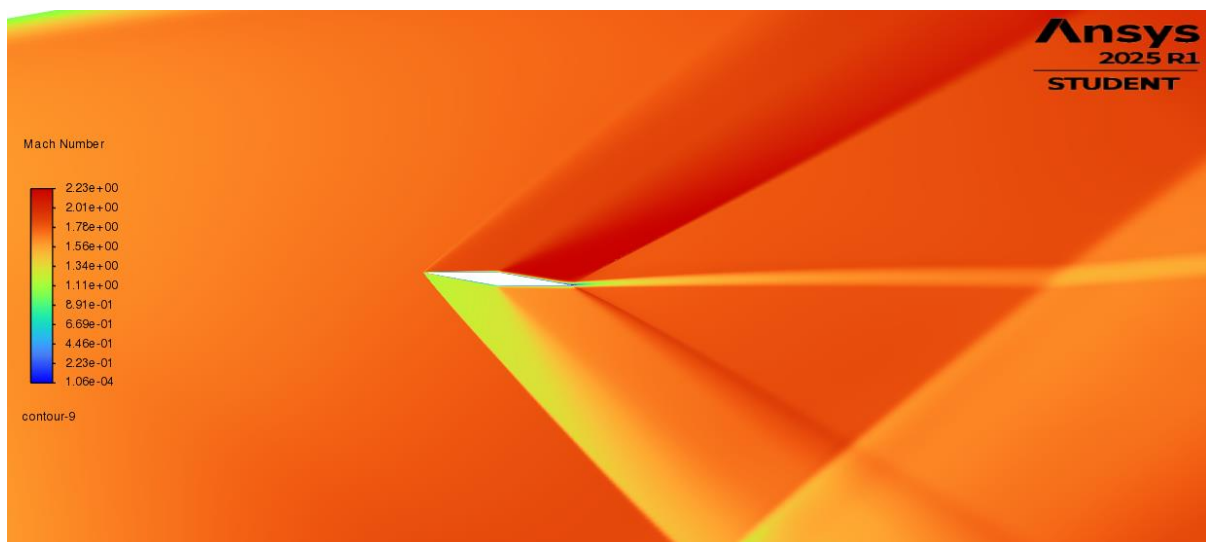


Figure 9 Mach Number Contour Plot

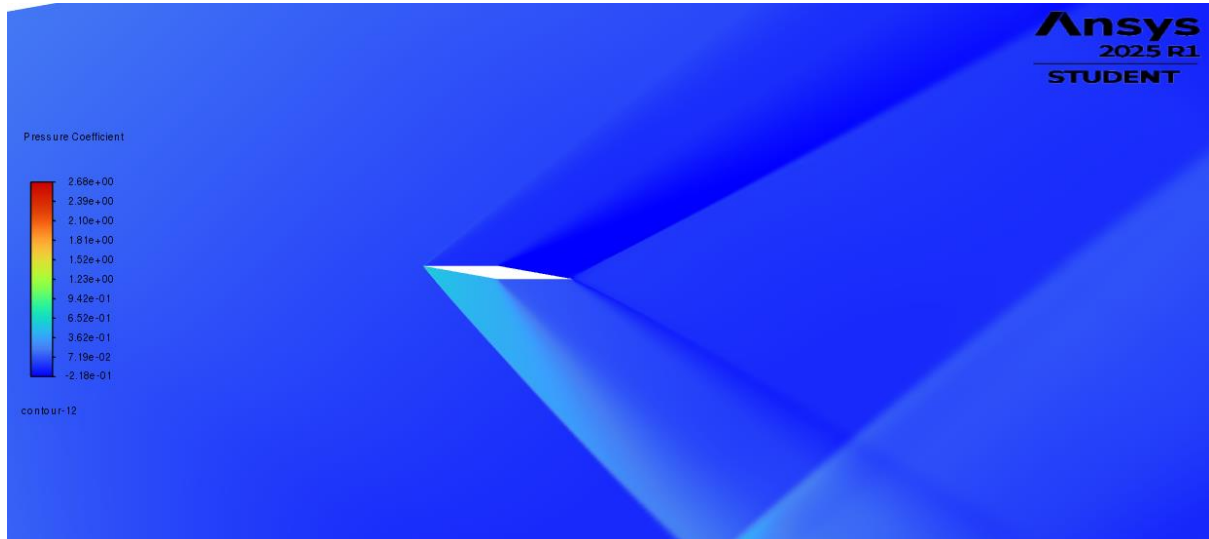


Figure 10 - Pressure Coefficient Contour Plot

Figure 9 displays the Mach number distribution. The undisturbed flow upstream approaches the aerofoil at the specified Mach 1.8 (indicated by the orange/yellow region). A distinct **oblique bow shock** is visible emanating from the leading edge on both the upper and lower surfaces, characterised by a sharp decrease in Mach number (transition to a deeper hue of orange) as the flow is compressed and turned. Following the initial wedge surfaces, **Prandtl-Meyer expansion fans** originate from the shoulder corners (approx. mid-chord). These are identified as regions where the Mach number increases smoothly (transition to red) as the flow accelerates around the convex corners. A higher Mach number **wake region** is evident downstream of the trailing edge. The angles of the shock waves and the spreading of the expansion fans are clearly visualised.

Figure 10 presents the pressure coefficient (C_p) contours. This non-dimensional representation mirrors the static pressure field. High positive C_p values (red region, max ≈ 2.68) confirm the significant compression on the lower leading surface. Lower, potentially negative, C_p values (blue region, min ≈ -0.22) are observed on the upper leading surface. The expansion fans are again visible as regions where C_p decreases sharply.

Collectively, these contour plots provide a comprehensive visualisation of the supersonic flow phenomena, clearly identifying the locations and nature of the shock waves and expansion fans generated by the aerofoil at the specified angle of attack.

3.4 Pressure Data Extraction

To enable quantitative comparison with theoretical and experimental results, the pressure coefficient (C_p) distribution along the aerofoil's upper and lower surfaces was extracted from the CFD solution. **Figure 11** plots this surface C_p data against the position along the wind tunnel axis (representing the chordwise position).

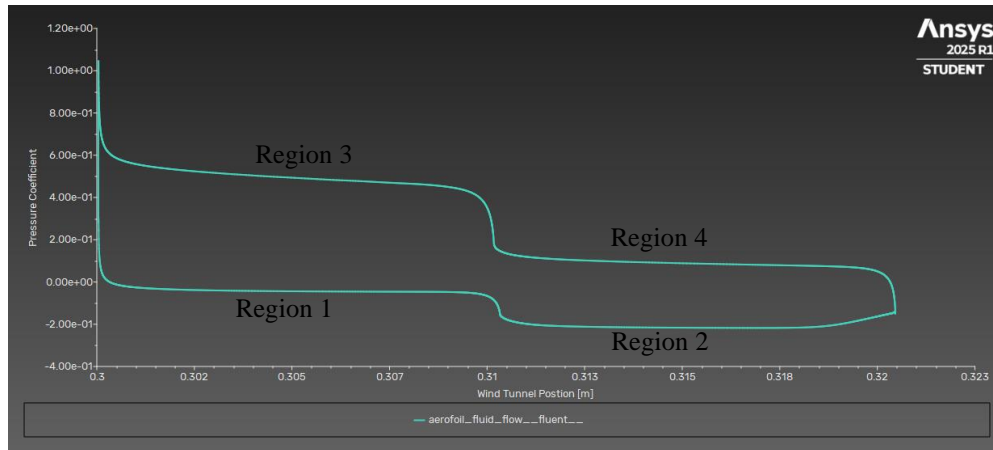


Figure 11 Pressure Coefficient vs. Position Plot as Figure

The plot clearly delineates the pressure distributions on the two surfaces:

- **Lower Surface (Upper Curve in Plot):** Starting from the leading edge (approx. $x=0.3\text{m}$), the C_p is high ($C_p \approx 0.6$) and relatively constant along the forward wedge surface. At the shoulder corner (approx. $x=0.31\text{m}$), a sharp drop in C_p occurs due to the Prandtl-Meyer expansion fan, reaching a lower value ($C_p \approx 0.15$) which remains relatively constant along the aft wedge surface until the trailing edge (approx. $x=0.32\text{m}$).
- **Upper Surface (Lower Curve in Plot):** The C_p starts near zero on the forward upper surface. A similar sharp drop in C_p occurs at the upper shoulder corner (approx. $x=0.31\text{m}$) due to the expansion fan, reaching negative values ($C_p \approx -0.2$). The C_p remains relatively constant along the aft upper surface.

The near-constant C_p values on the flat surfaces and the distinct drops at the expansion corners are characteristic features. The difference in C_p levels between the upper and lower surfaces highlights the aerodynamic loading. This extracted C_p distribution provides the necessary quantitative data for comparison with other analysis methods.

3.5 Angle Measurement

The angles of the dominant shock waves emanating from the leading edge were measured directly from the CFD post-processing results. This was done using the angle measurement tool within the visualisation software, which was applied to the Pressure Coefficient contours, as shown representatively in Figure 11.

The angles were measured relative to the incoming free-stream flow direction (horizontal, defined as 0°).

- **Upper Bow Shock Angle (β_{Upper}):** The angle of the lower shock wave was measured as approximately 35.4°

- **Lower Bow Shock Angle (β_{lower}):** The angle of the lower shock wave was measured as approximately 39.8°

The measured shock angles from the CFD visualisation appear symmetric in magnitude (approximately 37.7°) relative to the free-stream direction based on this measurement. These quantitative angle measurements from the CFD simulation will be compared against theoretical calculations and experimental data in the subsequent analysis sections.

4 Experimental Analysis:

The experimental phase of this investigation utilized the TecQuipment AF300 Intermittent Supersonic Wind Tunnel, a laboratory-scale facility designed for aerodynamic studies involving two-dimensional models in both subsonic and supersonic flow regimes up to Mach 1.8. This section details the experimental setup and presents the analysis of the data obtained.

4.1 Wind Tunnel Facility and Operation

The AF300 operates on an intermittent, induction-type principle. Unlike continuous tunnels that require large, constant power sources, or blowdown tunnels that directly expel high-pressure air, the AF300 uses a controlled supply of compressed air (provided by the separate AF300b unit, including storage vessels, compressor, and dryer) to induce ambient air through the test section.

The operation involves releasing compressed air strategically downstream of the test section (likely into a diffuser or ejector section). This high-speed injection creates a low-pressure region, drawing atmospheric air through the settling chamber, the convergent-divergent nozzle, and the working section where the model is mounted. This induction method generally produces a more stable, lower-turbulence flow in the test section compared to direct blowdown systems, which is advantageous for obtaining accurate aerodynamic measurements.

The supersonic Mach number in the test section is determined by the geometry of the interchangeable nozzle liners. For this study, the liners corresponding to a nominal Mach 1.8 were installed. The tunnel runs are intermittent, lasting for the duration allowed by the compressed air supply before the storage vessels need recharging. During a run, instrumentation, including pressure transducers connected to taps on the model and tunnel walls, and an optional Schlieren system for flow visualization, captures data related to the flow field around

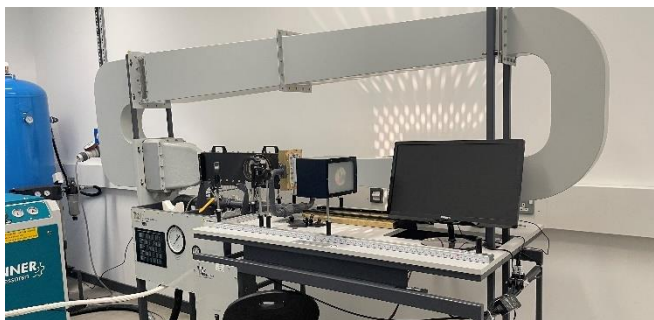


Figure 13 AF300 Wind Tunnel



Figure 12 Schlieren Image Setup

the test model. The experimental results discussed below were obtained using this facility configured for Mach 1.8 flow over the double-wedge aerofoil at a 5° angle of attack.

4.2 Schlieren Image Analysis

The experimental flow field around the double-wedge aerofoil at Mach 1.8 and 5° Angle of Attack was visualised using the Schlieren technique. A representative image obtained from the provided course resources is presented in Figure 14.

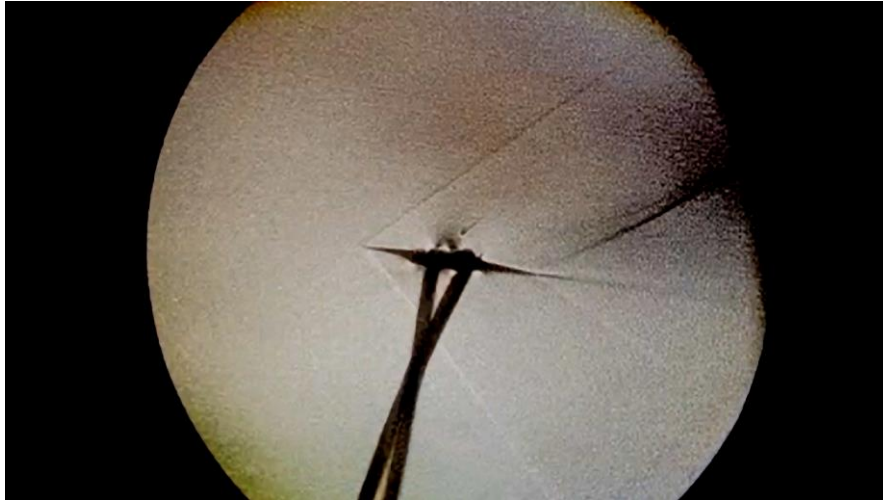


Figure 14 Schlieren Image

Figure 10 clearly shows the primary shock wave structures generated by the aerofoil interacting with the supersonic flow. Distinct **oblique shock waves** are visible originating from the leading edge. Consistent with the positive 5° angle of attack, the **lower shock wave appears noticeably steeper** (more inclined relative to the freestream direction) and more intense than the upper shock wave, indicating stronger compression on the lower surface. Expansion fans originating from the shoulder corners may also be faintly visible, although they are typically less sharply defined than shock waves in Schlieren images. The wake region downstream of the aerofoil can also be discerned.

Angle Measurement:

Angle measurements were performed directly on the Schlieren image, likely using image analysis software or digital measurement tools, to quantify the orientation of the leading-edge shock waves relative to the incoming freestream direction (assumed horizontal).

The measured angles are:

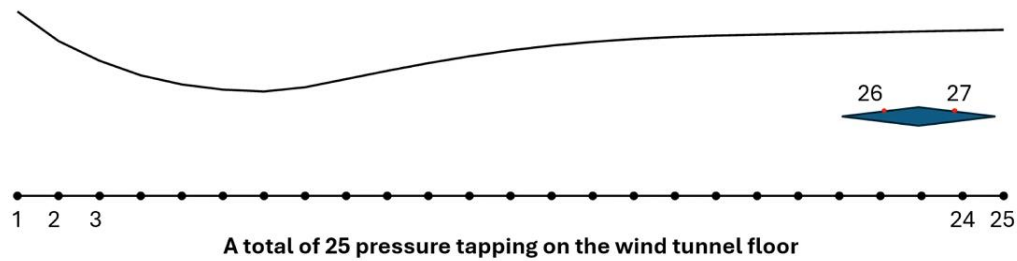
- **Upper Bow Shock Angle (β_{upper}) = 33.2°**
- **Lower Bow Shock Angle (β_{lower}) = 39.2°**

These experimentally measured angles provide quantitative data on the wave structure for direct comparison with theoretical predictions and CFD simulation results. Potential uncertainties in these measurements can arise from the clarity of the image, the finite thickness of the shock representation, and the precise determination of the freestream reference direction.

4.3 Pressure Data Analysis

Experimental pressure data for the double-wedge aerofoil at Mach 1.8 and 5° Angle of Attack was obtained from the provided course resources, which included time-logged pressure readings from multiple channels. Documentation regarding the pressure tap locations (referencing Figure [Insert Figure Number for the Mapping Image]) indicated that Tap 26 is located on the upper forward surface (leading edge wedge) and Tap 27 is located on the upper aft surface (trailing edge wedge) of the aerofoil model. Tap 28 measured the total pressure (P_0) in the settling chamber.

The Wind Tunnel Profile



Channel No.28 connects to the settling chamber and measures the total pressure.

Coordinates of the pressure tapping on the bottom floor.

	1	2	3	4	5	6	7	8	9	10	11	12	13
x	19.5	44.5	69.5	94.5	119.5	144.5	169.5	194.5	219.5	244.5	269.5	294.5	319.5
	14	15	16	17	18	19	28	21	22	23	24	25	
x	344.5	369.5	394.5	419.5	444.5	469.5	494.5	519.5	544.5	569.5	594.5	619.5	

Figure 15 Wind Tunnel Mapping by
AeroDynamics "<https://youtu.be/7-3yiOqREP0?si=DaHRoOMx9cJeoZDr>"

Analysis focused on the steady-state time point $t = 8.0$ seconds, where the tunnel operation appeared stable. At this time, the measured total pressure (P_0 , from Tap 28 via the 'Tunnel Reference Pressure' column) was:

$$P_0 = 8.0 \text{ bar}$$

The free-stream static pressure (P_∞) in the test section was calculated using the isentropic relation:

$$P_\infty = \frac{P_0}{\left[1 + \frac{\gamma - 1}{2} M_\infty^2\right]^{\frac{\gamma}{\gamma - 1}}}$$

$$P_\infty = \frac{8.0}{5.536} = 1.445 \text{ bar}$$

The pressure coefficient (C_p) at each tap was calculated as follows:

$$C_p = \frac{\left(\frac{P}{P_\infty} - 1\right)}{0.5 \cdot \gamma \cdot M_\infty^2}$$

$$C_{p,26} = -0.372$$

$$C_{p,27} = -0.373$$

The results for the aerofoil surface taps are summarised in Table 3.1 below.

Table 1 Experimental Pressure Coefficient Data for Aerofoil Taps ($t = 8.0s$)

Tap	Location	<i>Mach Number</i>	Calculated C_p
26	Upper Forward Surface	1.63	-0.372
27	Upper Aft Surface	1.65	-0.373

4.4 Discussion of Trends:

The experimental data provide C_p values at two distinct locations on the upper surface of the airfoil. Both measured points show negative C_p values ($C_p \approx -0.37$), indicating that the static pressure on the upper surface is significantly lower than the free-stream static pressure, as expected for the upper surface of an airfoil at a positive angle of attack in supersonic flow.

Interestingly, the C_p values measured on the forward wedge surface (Tap 26) and the aft wedge surface (Tap 27) are remarkably similar. This suggests that, according to these measurements, the pressure becomes relatively uniform along the upper surface after the initial leading-edge effects and the expansion fan located at the shoulder ($x/c = 0.5$).

This limited experimental pressure data provides valuable quantitative points for comparison with the theoretical predictions and the detailed surface pressure distribution obtained from the CFD simulation in the subsequent analysis sections.

5 Results Comparison and Discussion:

This section compares and discusses the results obtained from the theoretical analysis (using Shock-Expansion theory for $M=1.8$, $AoA=5^\circ$, with provided theoretical angles), the CFD simulation, and the experimental measurements (Schlieren imaging and pressure taps). The comparison focuses on key aerodynamic parameters: **shock wave angles** (Task 7) and surface pressure coefficient distributions (Task 8). Discrepancies between the methods are highlighted, and potential reasons are discussed.

5.1 Angle Comparison

The angles of the primary shock waves emanating from the leading edge are critical features of the supersonic flow field. These angles, as determined by each method, are summarized in Table 4.1.

Table 2 Comparison of Shock Wave Angles (Degrees)

Parameter	Theoretical	CFD	Experimental (Schlieren)
Upper Bow Shock Angle (β_{upper})	33.8° (Mach Wave)	35.4°	33.2°
Lower Bow Shock Angle (β_{lower})	43.03°	-39.8°	39.2°

Discussion of Angle Discrepancies:

Shock Angles:

- **Theory vs. CFD:** The theoretical analysis predicts an upper Mach wave ($\approx 33.8^\circ$) and a lower oblique shock ($\approx 43.2^\circ$), indicating asymmetry due to the 5° AoA. The CFD results (Upper $\approx 35.4^\circ$, Lower $\approx 39.8^\circ$) also show asymmetry, but with different magnitudes compared to theory. The CFD upper angle is slightly larger than the theoretical Mach wave angle, while the CFD lower angle magnitude (39.8°) is significantly smaller than the theoretical prediction (43.2°). Potential reasons for these differences include the inviscid assumption in theory versus viscous effects (boundary layer displacement altering effective deflection) and numerical diffusion/accuracy limitations in the CFD shock capturing.
- **CFD vs. Experiment:** The CFD upper shock angle (35.4°) is slightly larger than the experimental Schlieren measurement (33.2°). The CFD lower shock angle magnitude (39.8°) shows very good agreement with the experimental value (39.2°). The small difference in the upper angle could stem from minor variations in capturing the weaker upper wave in both CFD and experiment, or slight differences in real-world viscous effects versus the CFD model.
- **Theory vs. Experiment:** The experimental upper angle (33.2°) agrees remarkably well with the theoretical Mach wave angle ($\approx 33.8^\circ$), suggesting the upper leading-edge disturbance is indeed very weak. However, the experimental lower shock angle (39.2°) is considerably smaller than the theoretical prediction ($\approx 43.2^\circ$). This suggests that theoretical calculations overestimate the strength/angle of the lower shock, likely due to neglecting viscous effects present in the real flow.

Overall: All methods capture the presence of leading-edge waves. CFD and Experiment show asymmetric angles, although the CFD measured asymmetry differs from theoretical predictions. The experimental upper angle aligns well with theory (Mach wave), while the experimental lower angle aligns well with CFD but is less steep than predicted by theory. This suggests viscous effects significantly influence the lower shock angle.

5.2 Pressure Comparison

The pressure coefficient (C_p) distribution along the aerofoil surface provides insight into the aerodynamic loads. Figure 4.1 compares the C_p distributions obtained from theoretical calculations (using C_p values from the correct Shock-Expansion Theory for $M=1.8$, $AoA=5^\circ$: 0.000, 0.264, 0.264, -0.019), the CFD simulation, and the two experimental data points.

Discussion of Pressure Distribution Discrepancies:

- **Overall Trends:** All methods show relatively constant pressure on flat surfaces with sharp changes at the corners (shoulders). The CFD provides a continuous distribution, theory provides piecewise constant values, and the experiment provides data at two discrete points on the upper surface.
- **Upper Forward Surface ($0 < x/c < 0.5$):**
 - Theory predicts $C_p = 0.000$.
 - CFD shows C_p starting near zero and remaining close to zero before the shoulder.
 - Experiment (Tap 26, $x/c \approx 0.25$) measured $C_p \approx -0.372$.
 - *Comparison:* Major discrepancy between the experimental measurement and both theoretical/CFD predictions ($C_p \approx 0$). The experiment shows significantly lower pressure.

Potential reasons include experimental uncertainty, tap location inaccuracies, or complex leading-edge phenomena.

- **Lower Forward Surface ($0 < x/c < 0.5$):**
 - Theory predicts $C_p = 0.264$.
 - CFD shows $C_p \approx 0.6$.
 - *Comparison:* CFD predicts significantly higher compression than theory. This could be due to viscous effects or numerical aspects. No experimental data available.
- **Shoulder Corners ($x/c \approx 0.5$):**
 - Both theory and CFD predict sharp pressure changes due to waves/fans originating here. Theory predicts a pressure increase across the upper shoulder shock ($C_p=0.000$ to $C_p=0.264$) and a pressure drop across the lower shoulder expansion ($C_p=0.264$ to $C_p=-0.019$). CFD shows pressure drops on both surfaces ($C_p \approx 0$ to $C_p \approx -0.2$ Upper; $C_p \approx 0.6$ to $C_p \approx 0.15$ Lower).
- **Upper Aft Surface ($0.5 < x/c < 1.0$):**
 - Theory predicts $C_p = 0.264$ (due to the shock from the upper shoulder).
 - CFD shows $C_p \approx -0.2$.
 - Experiment (Tap 27, $x/c \approx 0.75$) measured $C_p \approx -0.373$.
 - *Comparison:* Theory significantly differs from both CFD and Experiment. CFD ($C_p \approx -0.2$) and Experiment ($C_p \approx -0.37$) both show negative pressure coefficients. The experimental value is lower than the CFD prediction. The similarity between the two experimental points suggests uniform low pressure, contrasting with the theoretical prediction of compression.
- **Lower Aft Surface ($0.5 < x/c < 1.0$):**
 - Theory predicts $C_p = -0.019$.
 - CFD shows $C_p \approx 0.15$.
 - *Comparison:* CFD predicts positive pressure, while theory predicts slightly negative C_p . No experimental data available.
- **Summary of Discrepancies:** Significant quantitative differences exist between all three methods, particularly in pressure levels. Theory struggles with upper surface predictions and the provided lower shock angle seems inconsistent. CFD captures qualitative pressure trends but shows quantitative deviations. Experimental data on the upper surface shows consistently lower pressure than predicted. Potential reasons include:
 - *Theoretical Assumptions:* Inviscid flow, sharp corners, potential inconsistency in provided theoretical angles.
 - *CFD Limitations:* Mesh resolution (no independence study), Spalart-Allmaras model accuracy, numerical diffusion. (*Self-Correction: Resolve C_p contour plot range inconsistency*).
 - *Experimental Uncertainties:* Limited taps assumed x/c locations, measurement accuracy, potential tunnel interference or model imperfections.

6 Conclusion

This study investigated the supersonic flow (Mach 1.8) over a double-wedge aerofoil at a 5° angle of attack using theoretical (Shock-Expansion Theory), computational (CFD with Spalart-Allmaras), and experimental (Schlieren, pressure taps) methods. The objective was to compare these approaches and understand the flow phenomena.

Key flow features, including leading-edge bow shocks/waves and shoulder waves/fans, were analysed. Comparison of leading-edge shock angles revealed interesting trends: the experimental upper angle (33.2°) closely matched the theoretical Mach wave prediction (33.8°), while the experimental lower angle (39.2°) agreed well with the CFD result (39.8° magnitude) but was significantly less steep than the theoretical prediction (43.2°). This suggests the theory accurately captures the weak upper disturbance but overestimates the lower shock strength, likely due to neglecting viscous effects, which are better represented (though perhaps not perfectly) by CFD and experiment.

Pressure coefficient comparisons highlighted significant quantitative differences. Theoretical predictions deviated considerably from CFD and experimental results, particularly on the upper surface. CFD captured qualitative pressure trends (compression on lower, expansion effects) but showed quantitative differences from theory. The limited experimental data (two points on the upper surface) indicated significantly lower pressures ($C_p = -0.37$) than predicted by either theory or CFD on the forward section, posing a point for further investigation.

The discrepancies underscore the limitations of each method. Theoretical analysis neglects viscosity. CFD results are subject to mesh resolution (no independence study performed), turbulence modelling, and numerical schemes. Experimental results are affected by measurement uncertainties and limited data points.

In conclusion, the multi-method approach provided valuable insights. While qualitative agreement on flow features exists, quantitative differences in shock angles and pressure distributions highlight the impact of viscosity and the inherent challenges in accurately modelling or measuring complex supersonic flows. The close agreement between experimental and CFD lower shock angles, contrasted with the theoretical overprediction, particularly emphasises the role of viscous phenomena.